Chemical Engineering Science 173 (2017) 374–383

Contents lists available at ScienceDirect

Chemical Engineering Science

journal homepage: www.elsevier.com/locate/ces

Analysis of powder rheometry of FT4: Effect of particle shape

Wenguang Nan [a,b], Mojtaba Ghadiri [a,*], Yueshe Wang [b]

[a] Institute of Particle Science and Engineering, School of Chemical and Process Engineering, University of Leeds, Leeds LS2 9JT, UK
[b] State Key Laboratory of Multiphase Flow in Power Engineering, Xi'an Jiaotong University, Xi'an 710049, China

HIGHLIGHTS

- Effects of particle shape on FT4 powder rheometry are analysed.
- A mathematical model is proposed to predict the flow energy of binary mixture.
- The flow energy and bulk friction coefficient are sensitive to particle shape.
- The flow energy correlates well with the shear stress in front of the blade.

GRAPHICAL ABSTRACT

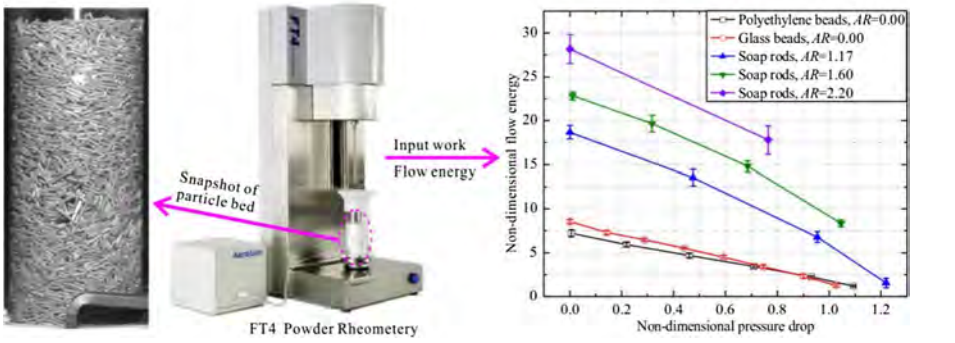

ARTICLE INFO

Article history:
Received 14 March 2017
Received in revised form 20 June 2017
Accepted 2 August 2017
Available online 9 August 2017

Keywords:
DEM
Rheology
Non-spherical particle
Rodlike particle
Flow energy

ABSTRACT

Particle shape has a strong influence on bulk powder flow and its associated rheology. It promotes mechanical arching and adversely affects fast feeding and dosing. We use the FT4 powder rheometer of Freeman Technology to experimentally characterise the particle flow as a function of the shear strain rate, and to predict its dynamics for rod-shape particles using the discrete element method. The results show a strong realignment of the orientation of particles in the horizontal plane as the bed is sheared by the blade motion. The flow energy required for agitating a bed of rodlike particles is much larger than that of spheres and it increases with the aspect ratio, due to a combined effect of the coordination number and excluded volume. The flowability of rodlike particles can be improved by the addition of spheres, and can be well predicted by the mathematical model developed in this work. The bulk friction coefficient of the binary mixture is a linear function of the volume fraction of its components. The flow energy correlates well with the shear stress arising in front of the blade, considering the effect of the bulk friction coefficient.

1. Introduction

Extreme particle shapes, such as acicular or platy, are often encountered in powder processing in a wide range of industrial applications, such as fast feeding, conveying, mixing and packaging processes. Particle shape has been shown to have a very important effect on the flow dynamics, such as the mixing rate and quality (Aramideh et al., 2015; Sinnott and Cleary, 2015; Xiong et al., 2015), particle breakage (Grof et al., 2007, 2011; Hua et al., 2013), and the flow pattern within hoppers (Höhner et al., 2015). Although the flow properties of spherical particles have been studied extensively by various researchers and reviewed by Campbell (2006), Delannay et al. (2007), Jop et al. (2006), Mort et al. (2015) and Tardos et al. (2003), the impact of particle shape on the bulk powder flow and associated rheology has only recently been analysed (Azema et al., 2007; Campbell, 2011; Cleary, 2008; Guo et al., 2012). Cleary (2008) simulated the plane Couette flow

* Corresponding author.
E-mail address: M.Ghadiri@leeds.ac.uk (M. Ghadiri).

http://dx.doi.org/10.1016/j.ces.2017.08.004
0009-2509/

of super-quadric shaped particles ($AR \leq 1.0$, where $AR = l_{max}/l_{min} - 1$ is the aspect ratio of particles and is 0.0 for spheres, l_{max} and l_{min} are the size of longer side and shorter side of particles, respectively), and found that such particle shapes could lead to much larger resistance to shear due to the interlocking between particles. Campbell (2011) simulated the simple shear flow of ellipsoidal particles ($AR = 0.25$, 0.5, 1.0) and showed that the quasi-static/inertial transition could occur at a much smaller solid fraction for ellipsoids ($AR = 1.0$) than that of spheres ($AR = 0.0$), as it was much easier to form force chains with ellipsoids. These studies revealed some important trends of the effect of particle shape on the bulk powder performance. However, in their simulations, the aspect ratios of particles are rather small (i.e., $AR \leq 1.0$). It is noteworthy that plane Couette flow and simple shear flow were used by Cleary (2008) and Campbell (2011), respectively. These shear conditions are far from the test conditions which can be replicated using existing instruments, and hence cannot be easily validated.

Conventional devices such as shear cells (Carson, 2015; Jenike, 1961; Schwedes, 2003) cannot easily be used for slender (acicular) particles with large aspect ratios, typically *AR* larger than about 1.0, due to the re-alignment of particles on the shear plane, effectively causing slip at the wall boundaries, an artefact of test method. Moreover, the effect of the strain rate cannot be analysed with standard shear cell methods. There are currently two proprietary instruments which are commercially available for the dynamic analysis of powder rheometry, the FT4 of Freeman Technology, Tewkesbury, UK, and the Anton Paar Powder Rheometer, Germany. Recently Salehi et al. (2016) have analysed the powder flow behaviour in the latter, whist we have paid more attention to the former (Hare et al., 2015; Nan et al., 2017) as it has received a great deal of attention (Han et al., 2011; Kinnunen et al., 2014; Osorio and Muzzio, 2013; Shur et al., 2008; Vasilenko et al., 2011; Zhou et al., 2010) and used widely in industry. However, its underlying powder mechanics has so far not been analysed extensively for fine and cohesive powders with extreme particle shapes, such as acicular or platy, hence the focus of this work. The FT4 instrument has a twisted blade which rotates whilst penetrating into a powder bed (Freeman, 2007). The input work required to drive the rotating blade into the powder bed is termed 'flow energy'. For spherical particles, Nan et al. (2017) have shown that the flow energy correlates with the shear stress on the blade and have proposed a linear correlation expressing the trend with the inertia number. Bharadwaj et al. (2010) simulated the blade resistance to powder flow in FT4, and showed that the flow energy was sensitive to the particle shape and friction coefficients. However, the strain rate and the stress within the particle bed were not characterised. In the case of non-spherical particles, the bulk powder flow is much more complicated, due to the interlocking between particles and the particle orientation.

We report on our analysis of the effect of particle shape on the dynamic behaviour of the particle bed using both experiments and numerical simulations with the discrete element method (DEM). The particle bed comprises rod-like particles, subjected to the standard FT4 testing procedure. The flow energy, microscopic structure, bulk friction and the resulting stresses within the powder bed are analysed. This provides a step towards understanding the influence of particle shape on the dynamics of FT4 powder rheometer.

2. Method

2.1. Experiments

In the FT4 powder rheometer, a stainless steel blade rotates and moves down and up through the powder bed in a cylindrical glass vessel at a pre-set speed (Freeman, 2007), as shown in Fig. 1 (a) and (b). Two kinds of particle shape are used: spheres and rods. The spherical particles are polyethylene and glass beads (designated as SA and SB, respectively). They are sieved and narrow sieve cuts of 0.5–0.6 mm for SA and 0.30–0.35 mm for SB are used. The rods are extruded soap cylinders with different aspect ratios. They are first roughly sieved into three size ranges designated as RA, RB and RC, and then measured by Morphologi G3. The dimensions of the particles are shown in Table 1, where the response angle is also

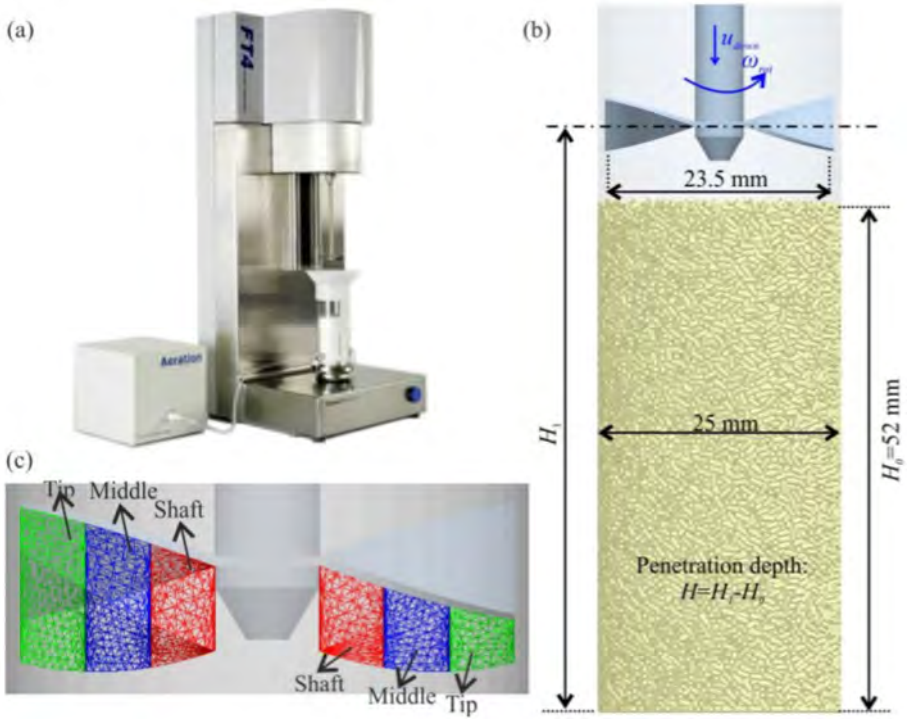

Fig. 1. Schematic illustration of (a) basic set up, (b) particle bed and (c) measured cells.

Table 1
The properties of particles in the experiments.

No.	Material	Length (L, mm)	Width (d, mm)	Aspect ratio ($L/d-1$)	Diameter (mm)	Repose angle (°)
SA	Polyethylene beads	–	–	0	[0.50–0.60][a]	19.1 ± 0.8
SB	Glass beads	–	–	0	[0.30–0.35][a]	21.4 ± 1.1
RA	Soap rods	1.33 ± 0.28	0.62 ± 0.06	1.17 ± 0.51	0.89 ± 0.10[b]	31.6 ± 0.5
RB	Soap rods	1.68 ± 0.29	0.66 ± 0.10	1.60 ± 0.58	1.03 ± 0.09[b]	32.5 ± 1.6
RC	Soap rods	1.94 ± 0.40	0.66 ± 0.12	2.00 ± 0.73	1.11 ± 0.14[b]	31.9 ± 1.1

±: standard deviation.
[a] Sieved by the standard sieves.
[b] Circle-equivalent diameter.

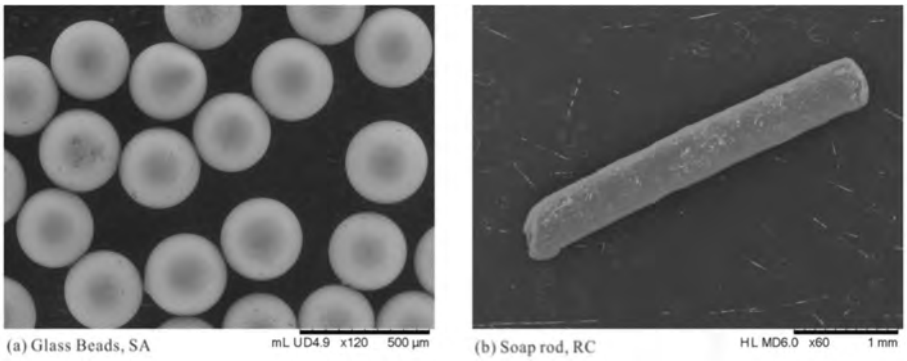

Fig. 2. The SEM images of spheres and rods.

included. A photograph of the particles taken by a Scanning Electron Microscope (SEM) is shown in Fig. 2. In the experiments, a conditioning cycle is first carried out to produce an initial particle bed with a reproducible packing state and low residual stress history, during which the blade rotates clockwise whilst moving downward and then upward. After this step the downward test is carried out, in which the blade rotates anti-clockwise and penetrates into the powder bed. In this way, the blade action is more compacting than slicing, resulting in shearing the bed under a normal load provided by the blade twisting angle. During the downward test, the torque T and axial force F are recorded. They are then used to calculate the total input work E, which is termed as the 'Flow Energy' for moving the powder:

$$E = \int_0^H \left(\frac{T}{R\tan\alpha} + F\right) dH \tag{1}$$

where R is the radius of the blade; α is the helix angle; $H = H_0\text{-}H_1$ is the penetration depth as shown in Fig. 1(b), where H_1 is the instantaneous vertical position of the blade and H_0 is the initial bed height. Here, the smaller glass vessel with 25 mm diameter and the corresponding 23.5 mm diameter blade are used. In the standard downward test, the blade moves with a constant downward speed, typically set around 0.1 m/s giving a dynamic helix angle of −5°. As a result, the downward translational velocity and rotational velocity of the blade are 0.00872 m/s and 8.48 rad/s, respectively. For varying the strain rate the impeller speed is changed in both rotational and downward motion so as to keep the helix angle constant. However, the impeller speed and helix angle are not changed in all downward tests in this work, thus, the translation and rotational velocities are also not changed. An upward gas flow with the maximum velocity of 0.16 m/s could be optionally introduced into the powder bed through a porous stainless steel disc at the base of the testing vessel. Besides the flow energy, the pressure drop of gas flow through the bed during test is also recorded. Before conducting any standard tests, a particle bed with a height of H_0 = 52 mm is generated through the conditioning cycle. The total flow energy corresponds to a penetration depth of 40 mm.

2.2. Simulations

The FT4 measurement process described above is also simulated by DEM, where particles are modelled as discrete phases and their motions are tracked individually by solving Newton's laws of motion (Cundall and Strack, 1979; Thornton, 2015). As the effect of gas flow on the particle flow in FT4 rheometer has been analysed for spherical particles by DEM-CFD simulation in our previous paper (Nan et al., 2017), the same has not been carried out for rodlike particles in this work, due to extremely long simulation time. Thus, only DEM simulation is carried out in following sections. The numerical simulation platform is developed based on EDEM^{TM} software provided by EDEM, Edinburgh, UK. For completeness, we only describe the key features of the simulation method as follows and further information could be found in Nan et al. (2016).

2.2.1. Numerical method

According to the DEM originally proposed by Cundall and Strack (1979), the movement of an individual particle could be reduced to the translational and rotational motion, described by:

$$m_i \frac{d\boldsymbol{v}_i}{dt} = \sum \boldsymbol{F}_{c,i} + m_i\boldsymbol{g} + \boldsymbol{f}_{pf,i} \tag{2}$$

$$\frac{d(\boldsymbol{I}_i \cdot \boldsymbol{\omega}_i)}{dt} = \boldsymbol{R}_i \cdot \left(\sum \boldsymbol{M}_{c,i} + \boldsymbol{M}_{pf,i}\right) \tag{3}$$

where m_i, $\boldsymbol{I}_i$, $\boldsymbol{v}_i$ and $\boldsymbol{\omega}_i$ are the mass, moment of inertia, translational velocity and angular velocity, respectively; $\boldsymbol{F}_{c,i}$ is the contact force, originating from particle interactions with neighbouring particles or wall; $\boldsymbol{M}_{c,i}$ is the contact torque, arising from the tangential and normal contact force; $\boldsymbol{f}_{pf,i}$ and $\boldsymbol{M}_{pf,i}$ are the fluid-particle interaction force and fluid induced torque on the particle, respectively, and they are not considered in this work; $\boldsymbol{R}_i$ is the rotation matrix from the

global to the local coordinate system. The calculation of the rotation expressed by Eq. (3) is accomplished in a local coordinate system which is a moving Cartesian coordinate system fixed to the rod and whose axes are superposed by the axes of inertia, as shown in Fig. 3, where the aspect ratio AR is defined as the ratio of the length L to the diameter $d = 2R$. Spherical shape may be regarded as two overlapping spheres, for which $L = 0$. The transformation of the angular velocity and torque between the local and global coordinate systems can be realized by the rotation matrix.

As introduced by Favier et al. (1999), the clumped sphere model is adopted to describe the interaction between rods. In this model, the rigid rod is assumed to be a chain of spheres, centres of which are located at the symmetry axis of the rod, as shown in Fig. 3. Thus the possible interactions between any two rods can be simplified as that of spherical particles, which is described by Hertz-Mindlin contact model. It should be noted that there are no inter-sphere forces between the spheres in the same rod. Obviously, the difference between the real rod and one represented by the clumped spheres can be adjusted by controlling the separation distance fraction of neighbouring spheres ($\delta = x/2R$, the ratio of the normal overlap of two adjacent spheres to the diameter of the rod). Generally, $\delta = 0.5$ is sufficiently large to give an accurate representation of the real rod, while providing reasonable computational time, as suggested by Grof et al. (2007, 2011) and Nan et al. (2014).

Practically, a clumped sphere represented rod may have multiple collision points with another one, which may deviate from the fact two real cylinders with hemi-spherical caps could make contact by only one contact point or a contact line (Kodam et al., 2010a,b). As a result, the simulated restitution coefficient of the whole rod will depend on the number of contact points and eventually the number of its sphere elements. For example, if the axes of the two sphere-represented rods in contact are parallel, the collision points will be more than one, resulting in an over-damped collision process. To reduce this deviation as much as possible, a collision factor is introduced, which is equal to the inverse of the number of collision points between two sphere-represented rods. All possible collision forces at these collision points are multiplied by this collision factor, and eventually summed up on the two sphere-represented rods. Of course, if there is only one collision point between these two rods, it is equal to the treatment of the conventional clumped sphere model.

2.2.2. Simulation conditions

The simulations use the same geometry of FT4 vessel and blade and the same blade speed as the experiments, as shown in Fig. 1(b). Using the poured packing method, particles ($AR = 0$, 1.5, 3.0) with a flat distribution of volume-equivalent diameters in the size range

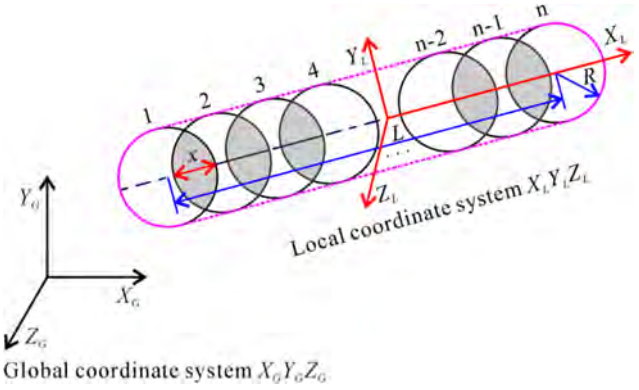

Fig. 3. The representation of the global and local coordinate systems for clumped sphere represented rod.

of 0.85–1.0 mm are generated to form a packed bed, and then the particles above the height of 52 mm are removed to obtain a constant bed height for particles with different aspect ratios. As the packed bed is in a reproducible packing state with low residual stresses, the bed preparation procedure (namely the conditioning step) is omitted in the simulations to reduce the computational time, following Hare et al. (2015) and Nan et al. (2017). The number of particles in the bed is around 36,000 and its exact value depends on the aspect ratio of particles. For the particles with aspect ratio of 0.0, 1.5 and 3.0, the particle number is 36,000, 38,274 and 34,927, respectively, and the corresponding porosity of the initial particle bed is 0.410, 0.379 and 0.434, respectively. Preliminary work not reported here showed little variations in the bed porosity, as a sufficiently large number of particles are used, so the results have a high repeatability. The material properties and interaction parameters in the simulations are listed in Tables 2 and 3, respectively, based on the work of Nan et al. (2017). Due to the interlocking between particles, rodlike particles are much less sensitive to the tip speed compared to spheres. Thus, we only focus on the effect of particle shape on the dynamics of FT4 rheometer in the simulations. To investigate the effect of the orientation/structure of the initial bed on the flow energy, one particular case is also used, where the orientation of particles generated to pack into the initial bed is vertical. Besides rodlike particles, the flow behaviour of the binary mixture of spherical and rodlike particles is also analysed. Nan et al. (2017) showed that the flow energy is correlated with the shear stress and strain rate by which the flow regime could be mapped out. By increasing the tip speed to 0.25 m/s, almost the same flow energy is obtained, suggesting that the particle flow in this work is in quasi-static flow regime, which is not shown here for brevity.

3. Experimental results

Compared to the snapshots of particle bed of spherical beads whilst the impeller is penetrating it, the rodlike particles show several differences as observed from Fig. 4: 1) besides the particle position, the particle orientation changes with the blade motion; 2) due to the interlocking between rodlike particles, there are dilute regions behind the impeller blade, as the void caused by the forward blade motion could not be immediately filled by the particles. This behaviour is more significant when the blade moves up after the downward test.

The variation of the total flow energy with the air pressure drop for different particles is shown in Fig. 5, where the non-dimensional flow energy E^* and pressure drop ΔP^* are defined as:

$$E^* = \frac{E}{(m_b g H)_{\max}} \tag{4}$$

$$\Delta P^* = \frac{\Delta P}{mg/S} \tag{5}$$

where m_b is the total particle mass above the blade; mg is the total weight of the particle bed; S is the cross-area of the vessel. Due to differences in surface properties, there is a difference between the flow energy of the two kinds of spherical beads, particularly for no or little air flow, where the frictional effect dominates. Compared

Table 2
Material properties in simulations.

Material property	Particles	Impeller blade	Cylindrical vessel
Density, ρ (kg/m^3)	1000	7800	2500
Shear modulus, G (Pa)	1×10^8	7.3×10^{10}	2.4×10^{10}
Poisson ratio, ν	0.35	0.3	0.3

Table 3
Contact interaction parameters in simulations.

Interaction property	Particles-particle	Particle-blade/vessel
Friction coefficient, μ	0.5	0.25
Restitution coefficient, *e*	0.6	0.6

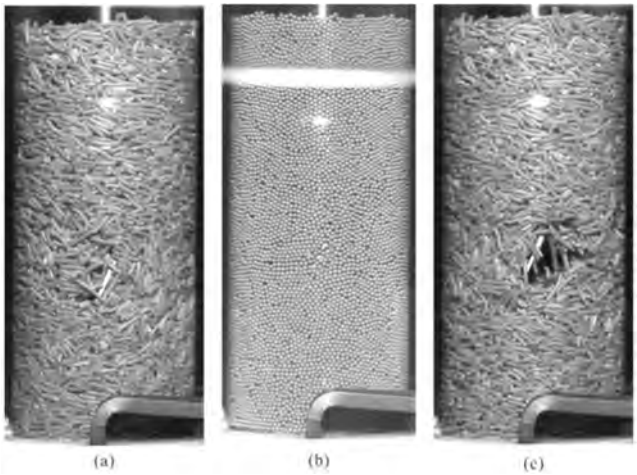

Fig. 4. The snapshots of particle bed for (a) rodlike particles during downward test, (b) spheres and (c) rodlike particles when the blade moves up after the test.

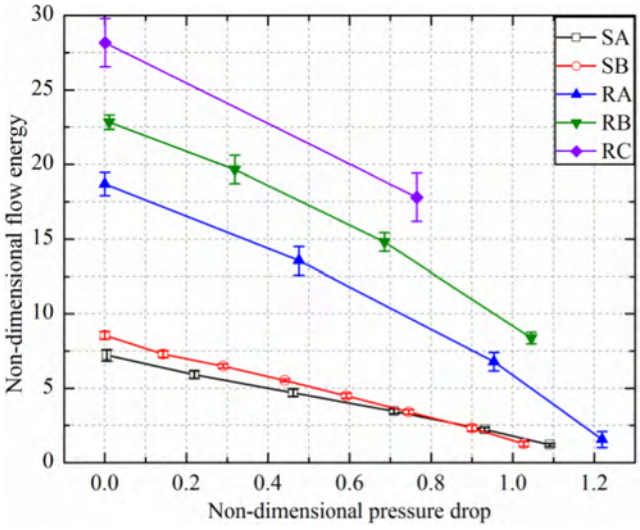

Fig. 5. The variation of the flow energy with pressure drop.

to the flow energy of spherical beads, the corresponding value of rodlike particles is much larger. For example, the flow energy of particles RB ($AR = 1.6$) is about 3.1 times that of particles SA ($AR = 0.0$) and 2.7 times that of particles SB ($AR = 0.0$). With the increase of the aspect ratio of rodlike particles, the flow energy also increases but its extent is less than the corresponding value when the particle shape changes from spherical to rodlike shape. When the gas flow is introduced, the total flow energy is reduced, as the bed weight is partially supported by the air drag. The difference of the flow energy between particles with different aspect ratios decreases as the air flow rate is increased. For spherical beads, the reduction of the flow energy is almost linear with the pressure drop, whilst for rodlike particles, the rate of the reduction of the flow energy (i.e. the slope) increases slightly with the pressure drop. For rodlike particles, at higher air flow rates, the interlocking between particles is weakened and thus the particles are easier to be sheared by the blade motion. Due to the re-orientation of particles, the microscopic structure of the particle bed changes with the blade motion, influencing the particle behaviour in the downward test. Therefore, large fluctuation could be observed in the flow energy of rodlike particles.

4. Simulation results

The impeller motion mainly affects the particles locally around the blade, whilst particles remote from the impeller are essentially stationary. Due to the blade motion, the orientation of particles changes with the penetration depth especially around the blade. The particle flow in front of the blade could be the main influencing factor of particle behaviour in FT4. Thus, the measurement cells (shaft, middle and tip) in front of the blade, spanning the width of the blade, are considered in the analysis following the approach of Hare et al. (2015) and Nan et al. (2017), as shown in Fig. 1(c). The microscopic structure of the particle flow shown in Fig. 4 is simulated and the coordination number and orientation angle are determined. The coordination number is defined as the number of particles in contact with the considered particle. The orientation angle is defined as the angle between the axis of rodlike particles and the vertical direction. Due to the symmetry, the orientation angle is calculated in [0°, 90°] for simplicity.

The variation of the mean coordination number with the aspect ratio is shown in Fig. 6 and its probability distribution is shown in Fig. 7. The mean coordination number in the measurement cells is averaged for the last 20 mm penetration depth, as suggested by Nan et al. (2017). For the initial bed, as the aspect ratio changes from 0.0 to 1.5, the mean coordination number increases from 4.8 to 6.4. With further increase of the aspect ratio, the mean coordination number shows a slight decrease, due to the effect of excluded volume defined as the volume around an object, in which the centre of another similarly shaped object is not allowed to penetrate (Balberg et al., 1984). The trend shown in Fig. 6 is consistent with the packing of rodlike particles, in which the mean coordination number firstly increases sharply to a maximum value and then decrease gradually, as the aspect ratio increases from 0.0 (spheres) to large value such as 20 (Wouterse et al., 2009). As the particle bed is agitated by the blade, it becomes looser locally, resulting in the decrease of the mean coordination number. In the measurement cells, with the increase of the aspect ratio, the mean coordination

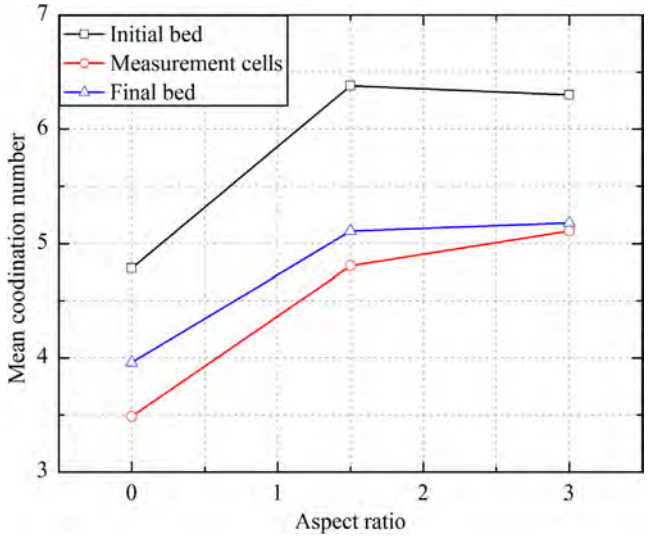

Fig. 6. The variation of the mean coordination number with aspect ratio.

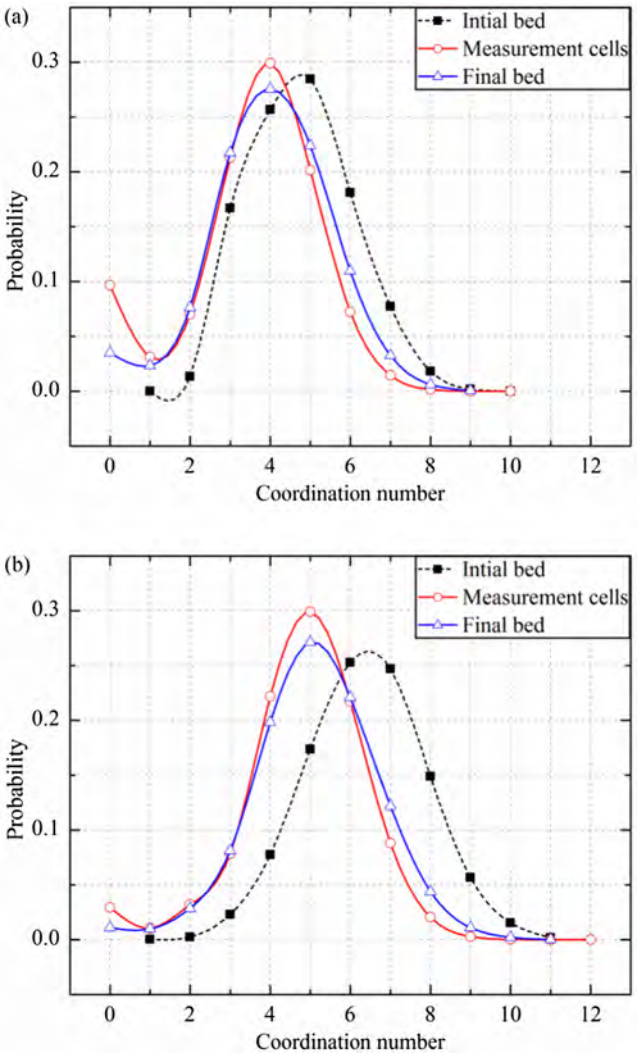

Fig. 7. The probability distribution of the coordination number (a) $AR = 0$ and (b) $AR = 1.5$.

number increases sharply and then slightly. Correspondingly, the distribution shown in Fig. 7 moves to the left, with more particles having a coordination number with low value. For spherical particles, almost 10% of particles have no contacts with neighbours. Due to the effect of excluded volume, the rodlike particles have less freedom to move. As a result, the rodlike particles have less free-moving particles ($CN = 0$) in the measurement cells than that of spherical particles. As the blade moves away, the particles pack again due to the gravity. Therefore, the mean coordination number in the final bed is larger than that in the measurement cells. Correspondingly, the distribution moves to right slightly and the probability of $CN = 0$ is greatly reduced. This trend is more significant for spherical particles.

The blade motion has a large influence on the evolution of particle orientation. The orientation of particles at the slice of $H = H_{max}/2$ before and after test is shown in Fig. 8. On the horizontal plane, the particle axes are almost randomly distributed in the initial bed as a consequence of filling; as the particles are generated, they fall on to the bed surface and assume a random orientation on the horizontal plane as shown in Fig. 8(a). They realign on shearing by the blade, and their orientation on the horizontal plane becomes almost tangential. The particle colour in Fig. 8 shows the orientation angle with the vertical direction, θ. Most particles in

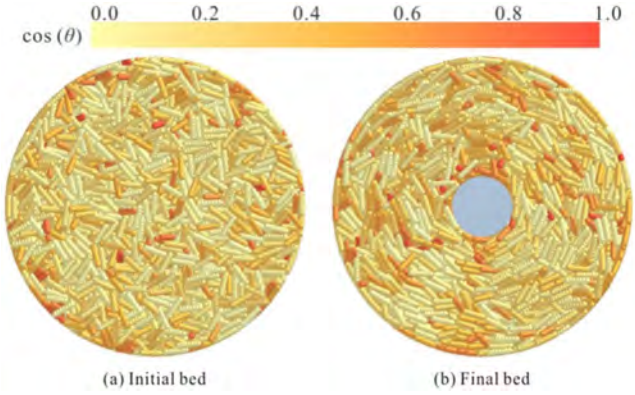

Fig. 8. The orientation of particles on the horizontal plane.

the initial bed lay horizontally ($\cos\theta = 0$), but the degree of this horizontal alignment is reduced in the final bed, as the blade shears the bed, the particles go over it and tumble down behind it, and their orientation becomes more random as shown in Fig. 8(b) by the increase in red colour.

The distributions of vertical orientation angle of particles in the initial particle bed as well as the final bed are shown in Fig. 9, where the x-axis is divided into 20 bins. The mean values of the vertical orientation angle of particles, $\langle\cos\theta\rangle$, are given in Table 4 and $\langle\cos\theta_i\rangle$ in Fig. 9 is referred to the value in the initial bed. Two cases are considered, one is where the particles have a random distribution of vertical orientation angle when they are released. However, most lie horizontally when settled, as shown in Fig. 10 (a). This is referred to as the 'standard' case and is always used if not specified. The second case is a particular one, where the particles are all released vertically ($\cos\theta = 1$), as shown in Fig. 10(b). It is intuitively expected that for this particular case $\langle\cos\theta\rangle$ is much larger than zero when particles have settled, i.e. less horizontal alignment in the initial bed than that of the standard one. As shown in Fig. 9, for the initial beds, the peak being near $\cos\theta = 0$ confirms the horizontal alignment of most particles in the bed, but $\cos\theta$ increases with the aspect ratio. As the particle bed is agitated by the blade, the degree of horizontal alignment of rodlike particles is reduced (i.e. less probability at $\cos\theta = 0$), resulting in a more random distribution of the angles between the rod axis and vertical direction for both particles with $AR = 1.5$ and 3.0. Compared to the standard case (i.e., $AR = 1.5$, $\langle\cos\theta_i\rangle = 0.316$), a much less hori-

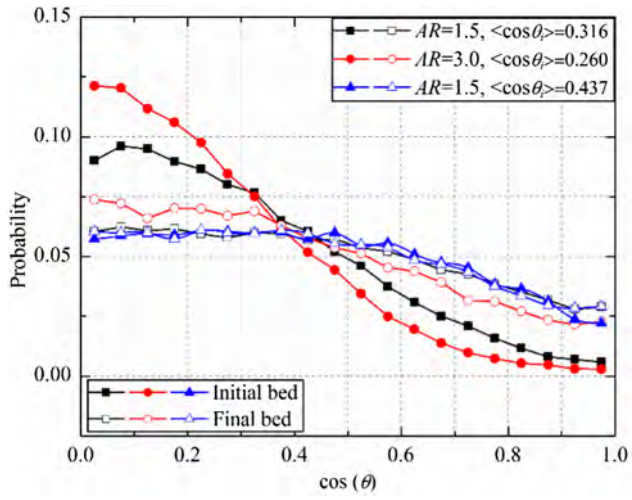

Fig. 9. The probability distribution of the orientation angle.

Table 4
Mean value of the orientation angle.

$\langle\cos\theta\rangle$	Initial bed	Measurement cell	Final bed
AR = 1.5, standard	0.316	0.482 ± 0.017	0.437
AR = 3.0, standard	0.260	0.499 ± 0.025	0.397
AR = 1.5, particular	0.437	0.468 ± 0.018	0.438

zontal alignment of particles in the initial bed and a smaller difference of the probability distribution of the orientation angle between the initial and final beds are found in the particular case (i.e., AR = 1.5, $\langle\cos\theta_i\rangle$ = 0.437). The mean vertical orientation angle of particles averaged in the three measurement cells fluctuates with the blade motion, and its averaged value as well as the standard variation along the last 20 mm penetration depth is also shown in Table 4. $\langle\cos\theta\rangle$ is the largest in the measurement cells; this indicates that particles in the initial particle bed assume a less horizontal alignment on shearing, and then align again into horizontal direction as the blade moves away.

4.1. Flow energy

The evolution of the simulated flow energy E^* with the penetration depth is shown in Fig. 11, where $\langle\cos\theta_i\rangle$ is the mean vertical orientation angle of particles in the initial bed and specified to be 0.5 for spherical beads as they do not have preferred orientation. As the impeller is driven into the particle bed, the flow energy of the rodlike particles is always larger than that of the spherical particles. For example, the total flow energy of rodlike particles (AR = 1.5) is about 2.6 times that of spherical beads (AR = 0.0) at the maximum penetration depth. The strong dependence of flow energy on the aspect ratio is mainly ascribed to the combined effect of the coordination number and excluded volume. Nan et al. (2017) have shown that the flow energy increases with the coordination number if the tip speed is kept constant. In both AR = 1.5 and AR = 3.0 cases, the mean coordination number is much larger than that of spherical beads. A large excluded volume promotes large interlocking and thus a large resistance to the shear deformation. These mechanisms contribute to the increase of the flow energy when the particle shape changes from spherical to rodlike. On the other hand, for comparison between the two cases of AR = 1.5 and AR = 3.0, the coordination number changes little, whilst the flow energy increases. This trend suggests that the flow energy is controlled by the excluded volume V_{ex}/V_p when the aspect ratio is large. It is intuitively expected that as the aspect ratio is increased further, the strong interlocking due to the large excluded volume could reduce the coordination number of particles. In this case, the effect of increased excluded volume can surpass the effect of the decreased coordination number, resulting in the increase of flow energy.

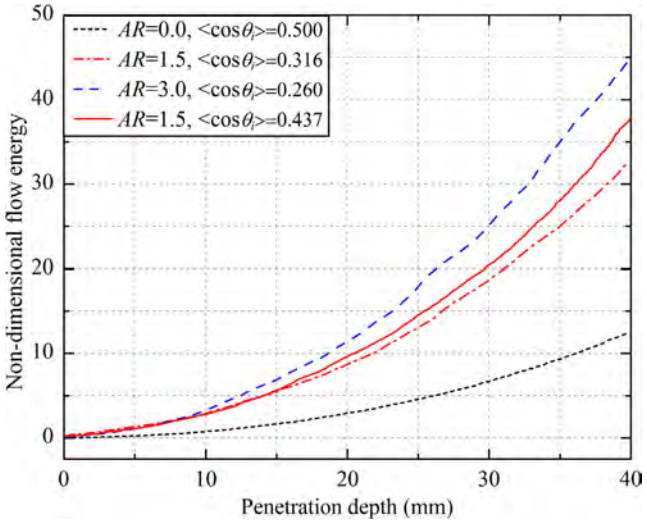

Fig. 11. The variation of flow energy with the penetration depth.

Particle orientation also plays an important role in the flow energy. Compared to the standard case (i.e. AR = 1.5, $\langle\cos\theta_i\rangle$ = 0.316), a slightly larger flow energy can be found in the particular case (i.e. AR = 1.5, $\langle\cos\theta_i\rangle$ = 0.437), although the mean coordination number in both cases changes slightly, which is not shown here for brevity. In this particular case, the total flow energy is about 3.0 times that of spherical beads (AR = 0.0). The reason for the increase of flow energy is presumably due to the shearing of the vertically-aligned rods and transformation of their orientation to a more random state. Clearly, the flow energy of rodlike particles depends on the orientation structure of the particle bed. This is consistent with the large fluctuation of flow energy in the experiment.

Due to the effect of particle orientation, the flow energy of rodlike particles with aspect ratio of 1.5 could be about 2.6–3.0 times of spherical particles. It is consistent with the experimental results, where the flow energy of particles RB (AR = 1.6) is about 3.1 times that of particles SA (AR = 0.0).

As discussed above, the flow energy increases with the aspect ratio. It may be possible to use spherical beads to improve the flowability of rodlike particles. The flow energy of the mixtures of rodlike particles (AR = 1.5) and spherical beads (AR = 0.0) for various volume fractions of spherical beads, x_f, is shown in Fig. 12. For the mixtures, the flow energy is less than that of rodlike particles but larger than that of spherical beads, along the penetration depth. It suggests that the flowability of rodlike particles could be much improved by the addition of spherical beads, as also shown previously by Elliott and Windle (2000). The total flow

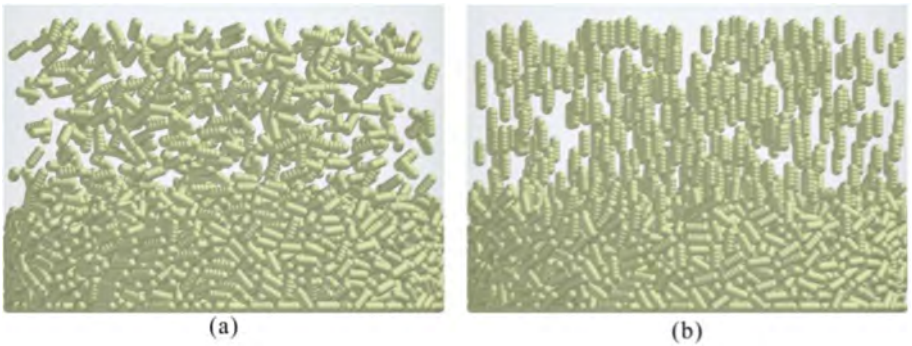

Fig. 10. Schematic diagram of the particles before packing in (a) standard case with random orientation and (b) particular case with vertical orientation.

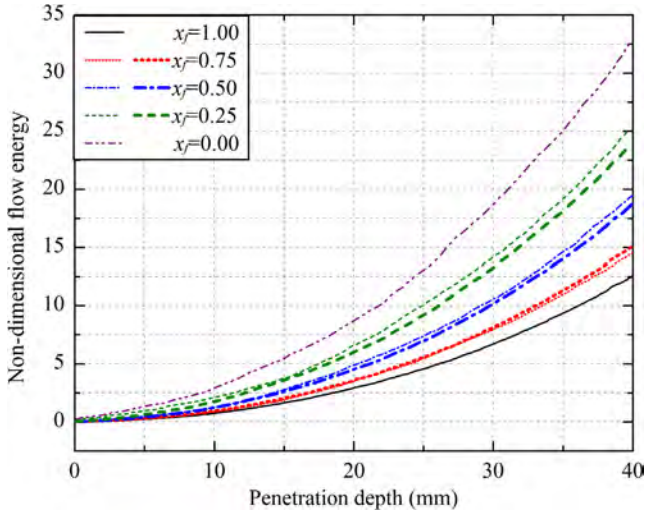

Fig. 12. The variation of the flow energy of mixtures (AR = 1.5 & AR = 0.0 at volume fraction, x_f, of spherical beads) with the penetration depth (thin lines: simulated results; thick lines: Eq. (6) with simulated E of the mixture).

energy E^*_{max} of mixtures of rods and spherical beads generated in DEM simulations is shown in Fig. 13, where the particles with the smaller aspect ratio are termed as "shorter particles". The reduction of total flow energy due to the addition of the spherical beads is more significant for rodlike particles with larger aspect ratio. The total flow energy of the binary mixture is a nonlinear function of the volume fraction of the shorter particles. These results indicate that the flow energy of the mixtures could be quantified by Eq. (6):

$$\frac{x_1}{\phi_1 E_1}+\frac{x_2}{\phi_2 E_2}=\left(\frac{x_1}{\phi_1}+\frac{x_2}{\phi_2}\right)\frac{1}{E} \tag{6}$$

where ϕ_1 and ϕ_2 are the sphericity of the components, as defined by the ratio of the surface area of volume-equivalent sphere to that of the actual particle; x_1 and x_2 (=1−x_1) are the volume fraction of the components; E_1 and E_2 are the flow energies of pure components, and E that of the mixture, all determined by simulations. Based on this equation, the variation of the flow energy with the penetration depth is shown as thick lines in Fig. 12. It suggests that the flow energy of the mixture can be well quantified by this equation along the penetration depth. The variation of the total flow energy with the volume fraction of the shorter particles as predicted by Eq. (6) is also shown in Fig. 13, following closely the actual simulated data.

4.2. Stress analysis

The stress analysis is also conducted for the particle flow immediately in front of the blade, within three measurement cells shown in Fig. 1(c). Here, the stress tensor is given by:

$$\sigma_{ij}=\frac{1}{V}\left(\sum_{p\in V} m_p \delta v_i \delta v_j+\sum_{c\in V} f_{ij}\cdot r_{ij}\right) \tag{7}$$

where V is the cell volume; m_p is the mass of particle p within the cell; δv_i and δv_j are the fluctuation velocities of particle p within the cell; f_{ij} is the contact force at contact c which is within the cell and r_{ij} is the corresponding branch vector between mass centre of particle i and that of particle j. Based on the stress tensor, the three principal stresses could be calculated: major one σ_1, intermediate one σ_2 and minor one σ_3. The normal stress p and shear stress τ are then given as:

$$p=\frac{\sigma_1+\sigma_2+\sigma_3}{3} \tag{8}$$

$$\tau=\frac{\sqrt{(\sigma_1-\sigma_2)^2+(\sigma_1-\sigma_3)^2+(\sigma_2-\sigma_3)^2}}{\sqrt{6}} \tag{9}$$

Similar to the flow energy, the normal and shear stresses also increase with the penetration depth. At the same penetration depth, both normal and shear stresses are the largest in the tip region and the smallest in the shaft region. Their relationship for rods with AR = 1.5 is shown in Fig. 14 along the whole length of the blade, where they are normalised by $(m_b g/S)_{max}$. The evolution of shear stress shows the same trend as of the normal stress in all measurement cells and could be quantified by the bulk friction coefficient $\mu_e = \tau/p$. The variation of the bulk friction coefficient $\mu_e = \tau/p$ with the volume fraction of the shorter particles is shown in Fig. 15. The bulk friction coefficient is much larger than that shown previously by Nan et al. (2017), where the value for the particle bed of spherical beads with different strain rate was always less than 0.41. It should be noted that the strain rate in this work is almost the same in all cases. Thus, the results also suggest that the bulk friction coefficient is more sensitive to the particle shape

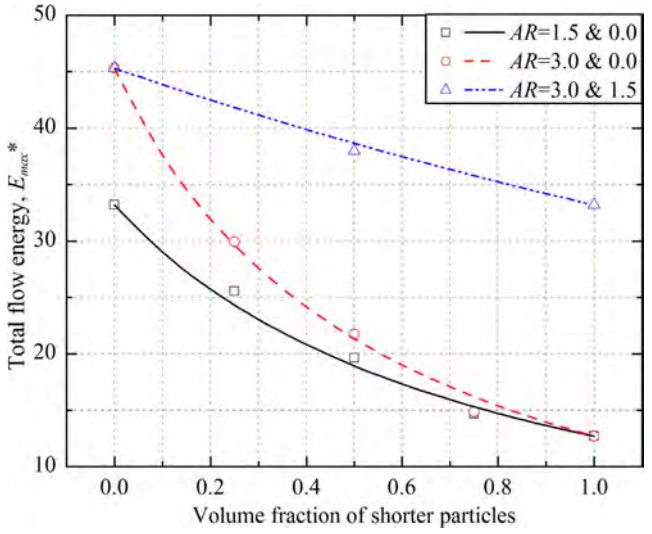

Fig. 13. The variation of flow energy of mixtures with the volume fraction of the shorter particles (data points: simulated results; lines: Eq. (6)).

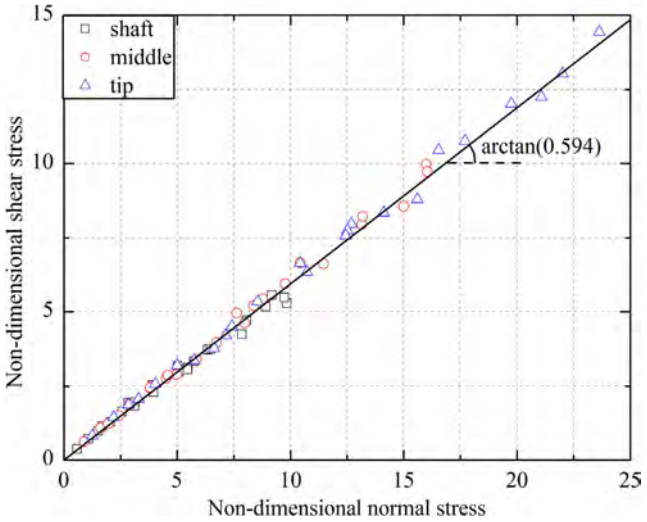

Fig. 14. The relationship between the normal and shear stresses for rodlike particles with AR = 1.5 across the whole blade length.

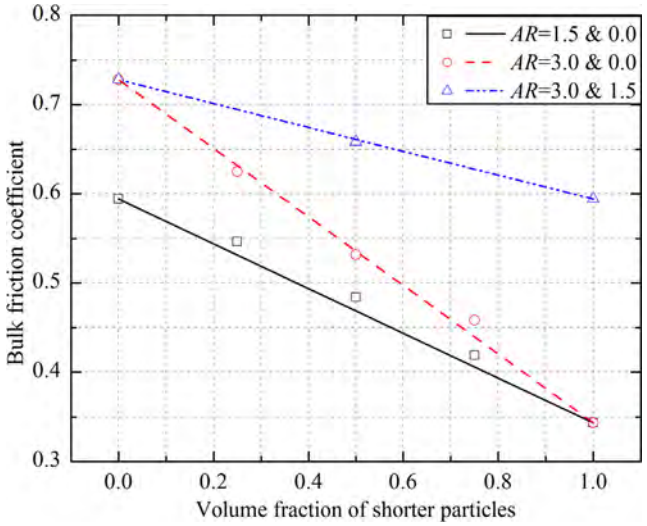

Fig. 15. The variation of bulk friction coefficient of mixtures with the volume fraction of the shorter particles (data points: simulated results; lines: fitting line).

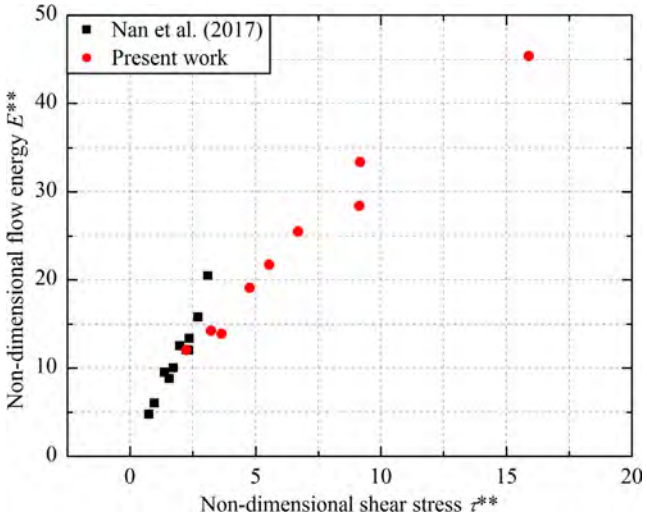

Fig. 16. The variation of the flow energy with averaged shear stress in the measurement cells for rodlike particles (present work) and spherical particles (Nan et al. (2017)).

than the strain rate. The bulk friction coefficient increases with the aspect ratio and can be reduced by the addition of spheres. It shows a linear function on the volume fraction of shorter particles.

Nan et al. (2017) showed that the non-dimensional flow energy ($E^{**} = E/m_b gH$) and shear stress ($\tau^{**} = \tau S/m_b g$) had a weak dependence on the penetration depth. They used the averaged value of the last 20 mm of penetration depth for E^{**} and τ^{**}, and found E^{**} correlated well with the averaged value τ^{**} in the three measurement cells in front of the blade, which is also the case in this work as shown in Fig. 16. However, the whole trend shows that E^{**} is not linear with τ^{**}, as the bulk friction of rodlike particles is much larger than that of spherical beads. It suggests that the bulk friction coefficient should be taken into account when considering the relationship between the shear stress and flow energy.

5. Conclusions

The rheological behaviour of rodlike particles subjected to shearing flows by an impeller has been analysed using the FT4 instrument by a combination of experimental measurements and DEM simulations. The effects of aspect ratio on the particle flow have been analysed and quantified in terms of the microscopic structure, flow energy and stresses. The main results from the present study are summarised as follows:

(1) The flow energy required for agitating bed of rodlike particles is much larger than that of spheres and depends on the aspect ratio. It is the combined effect of the coordination number and excluded volume. The flow energy of rodlike particles is also affected by the microscopic structure of the initial bed.
(2) The flowability of rodlike particles can be improved by the addition of spherical beads, and this improvement increases with the volume fraction of the spherical beads in the binary mixture. A mathematical model based on the particle shape is developed, and it could well predict the flow energy of the binary mixture.
(3) The bulk friction coefficient is sensitive to the particle shape, and could be reduced by the addition of spherical beads. The bulk friction coefficient of the mixture shows a linear function of the corresponding bulk friction coefficient of its pure components.
(4) The flow energy correlates well with the shear stress in front of the blade, and its value could be evaluated by the shear stress, considering the effect of the bulk friction coefficient.

Acknowledgments

The authors are grateful to the scholarship from China Scholarship Council (CSC) (Grant No. 201506280088) for the first author. We are thankful to DEM Solutions, Edinburgh, UK, for providing a special license for the EDEM software for use in this work, and also to Drs Colin Hare and Mehrdad Pasha for their generous help in setting up the computational facility, as well as Dr Tina Bonakdar for providing the experimental particles. We also thank Freeman Technology for making available an FT4 instrument for the experiment, as well as technical support from Dr Doug Millington-Smith.

References

Aramideh, S., Xiong, Q., Kong, S.-C., Brown, R.C., 2015. Numerical simulation of biomass fast pyrolysis in an auger reactor. Fuel 156, 234–242.
Azema, E., Radjai, F., Peyroux, R., Saussine, G., 2007. Force transmission in a packing of pentagonal particles. Phys. Rev. E Stat. Nonlin. Soft Matter Phys. 76, 011301.
Balberg, I., Anderson, C.H., Alexander, S., Wagner, N., 1984. Excluded volume and its relation to the onset of percolation. Phys. Rev. B 30, 3933–3943.
Bharadwaj, R., Ketterhagen, W.R., Hancock, B.C., 2010. Discrete element simulation study of a Freeman powder rheometer. Chem. Eng. Sci. 65, 5747–5756.
Campbell, C.S., 2006. Granular material flows – An overview. Powder Technol. 162, 208–229.
Campbell, C.S., 2011. Elastic granular flows of ellipsoidal particles. Phys. Fluids 23, 013306.
Carson, J.W., 2015. Limits of silo design codes. Practice Periodical on Structural Design and Construction 20, 04014030.
Cleary, P.W., 2008. The effect of particle shape on simple shear flows. Powder Technol. 179, 144–163.
Cundall, P.A., Strack, O.D.L., 1979. A discrete numerical model for granular assemblies. Géotechnique 29, 47–65.
Delannay, R., Louge, M., Richard, P., Taberlet, N., Valance, A., 2007. Towards a theoretical picture of dense granular flows down inclines. Nat. Mater. 6, 99–108.
Elliott, J.A., Windle, A.H., 2000. A dissipative particle dynamics method for modeling the geometrical packing of filler particles in polymer composites. J. Chem. Phys. 113, 10367–10376.
Favier, J.F., Abbaspour-Fard, M.H., Kremmer, M., Raji, A.O., 1999. Shape representation of axi-symmetrical, non-spherical particles in discrete element simulation using multi-element model particles. Eng. Comput. 16, 467–480.
Freeman, R., 2007. Measuring the flow properties of consolidated, conditioned and aerated powders - A comparative study using a powder rheometer and a rotational shear cell. Powder Technol. 174, 25–33.
Grof, Z., Kohout, M., Stepanek, F., 2007. Multi-scale simulation of needle-shaped particle breakage under uniaxial compaction. Chem. Eng. Sci. 62, 1418–1429.

Grof, Z., Schoellhammer, C.M., Rajniak, P., Stepanek, F., 2011. Computational and experimental investigation of needle-shaped crystal breakage. Int. J. Pharm. 407, 12–20.
Guo, Y., Wassgren, C., Ketterhagen, W., Hancock, B., James, B., Curtis, J., 2012. A numerical study of granular shear flows of rod-like particles using the discrete element method. J. Fluid Mech. 713, 1–26.
Höhner, D., Wirtz, S., Scherer, V., 2015. A study on the influence of particle shape on the mechanical interactions of granular media in a hopper using the Discrete Element Method. Powder Technol. 278, 286–305.
Han, X., Ghoroi, C., To, D., Chen, Y., Dave, R., 2011. Simultaneous micronization and surface modification for improvement of flow and dissolution of drug particles. Int. J. Pharm. 415, 185–195.
Hare, C., Zafar, U., Ghadiri, M., Freeman, T., Clayton, J., Murtagh, M.J., 2015. Analysis of the dynamics of the FT4 powder rheometer. Powder Technol. 285, 123–127.
Hua, X., Curtis, J., Hancock, B., Ketterhagen, W., Wassgren, C., 2013. The kinematics of non-cohesive, sphero-cylindrical particles in a low-speed, vertical axis mixer. Chem. Eng. Sci. 101, 144–164.
Jenike, A.W., 1961. Gravity flow of bulk solids. Bulletin No. 108, Utah State University.
Jop, P., Forterre, Y., Pouliquen, O., 2006. A constitutive law for dense granular flows. Nature 441, 727–730.
Kinnunen, H., Hebbink, G., Peters, H., Shur, J., Price, R., 2014. An investigation into the effect of fine lactose particles on the fluidization behaviour and aerosolization performance of carrier-based dry powder inhaler formulations. AAPS PharmSciTech 15, 898–909.
Kodam, M., Bharadwaj, R., Curtis, J., Hancock, B., Wassgren, C., 2010a. Cylindrical object contact detection for use in discrete element method simulations, Part II—Experimental validation. Chem. Eng. Sci. 65, 5863–5871.
Kodam, M., Bharadwaj, R., Curtis, J., Hancock, B., Wassgren, C., 2010b. Cylindrical object contact detection for use in discrete element method simulations. Part I - Contact detection algorithms. Chem. Eng. Sci. 65, 5852–5862.
Mort, P., Michaels, J.N., Behringer, R.P., Campbell, C.S., Kondic, L., Langroudi, M.K., Shattuck, M., Tang, J., Tardos, G.I., Wassgren, C., 2015. Dense granular flow - A collaborative study. Powder Technol. 284, 571–584.
Nan, W., Ghadiri, M., Wang, Y., 2017. Analysis of powder rheometry of FT4: Effect of air flow. Chem. Eng. Sci. 162, 141–151.
Nan, W., Wang, Y., Wang, J., 2016. Numerical analysis on the fluidization dynamics of rodlike particles. Adv. Powder Technol. 27, 2265–2276.
Nan, W.G., Wang, Y.S., Ge, Y., Wang, J.Z., 2014. Effect of shape parameters of fiber on the packing structure. Powder Technol. 261, 210–218.
Osorio, J.G., Muzzio, F.J., 2013. Effects of powder flow properties on capsule filling weight uniformity. Drug Dev. Ind. Pharm. 39, 1464–1475.
Salehi, H., Sofia, D., Lu, H., Schutz, D., Barletta, D., Poletto, M., 2016. Experiments and simulation of torque values of large and small particle size powders in Anton Paar Powder Cell using a commercial DEM simulation software. Powder, Granule and Bulk Solids: Innovations and Applications 5.
Schwedes, J., 2003. Review on testers for measuring flow properties of bulk solids (based on an IFPRI-Report 1999). Granular Matter 5, 1–43.
Shur, J., Harris, H., Jones, M.D., Kaerger, J.S., Price, R., 2008. The role of fines in the modification of the fluidization and dispersion mechanism within dry powder inhaler formulations. Pharm. Res. 25, 1631–1640.
Sinnott, M.D., Cleary, P.W., 2015. The effect of particle shape on mixing in a high shear mixer. Computational Particle Mechanics.
Tardos, G.I., McNamara, S., Talu, I., 2003. Slow and intermediate flow of a frictional bulk powder in the Couette geometry. Powder Technol. 131, 23–39.
Thornton, C., 2015. Granular Dynamics, Contact Mechanics and Particle System Simulations. Springer.
Vasilenko, A., Glasser, B.J., Muzzio, F.J., 2011. Shear and flow behavior of pharmaceutical blends - Method comparison study. Powder Technol. 208, 628–636.
Wouterse, A., Luding, S., Philipse, A.P., 2009. On contact numbers in random rod packings. Granular Matter 11, 169–177.
Xiong, Q., Aramideh, S., Passalacqua, A., Kong, S.-C., 2015. Characterizing effects of the shape of screw conveyors in gas-solid fluidized beds using advanced numerical models. J. Heat Transfer 137, 061008.
Zhou, Q., Armstrong, B., Larson, I., Stewart, P.J., Morton, D.A., 2010. Improving powder flow properties of a cohesive lactose monohydrate powder by intensive mechanical dry coating. J. Pharm. Sci. 99, 969–981.